KRONOS FUSION ENERGY

PAPER 2.7 · THE KRONOS 2026 SERIES

Free-Boundary Equilibrium and Ideal-MHD Stability of a Compact Spherical-Tokamak Breeder: Troyon, Mercier, Ballooning and External-Kink Margins with a Vertical-Stability Flag

A fusion design point is physical only if it corresponds to a self-consistent free-boundary equilibrium that is stable to the fast ideal-magnetohydrodynamic (MHD) modes. We...

Read it live — 3-D model · physics validator · film series

BY P I FORD AND G L KULCINSKI

2026 · EDITORIAL EDITION

THE OFFICIAL RECORD

What this document is, and how to read its numbers

This is a combined editorial. It gathers, in one volume, the two design studies Kronos Fusion Energy released in 2026 — a compact spherical-tokamak tritium/helium-3 breeder and a deuterium–helium-3 tandem-mirror generator — together with the intellectual-property estate, the people, and, in the internal edition, the full commercial case. The scientific text is the same text that appears in the arXiv preprints and the journal submissions; the editorial adds the apparatus a reader needs to hold the whole program at once, and nothing in the physics is altered to fit it.

THE HONESTY STANCE IS THE ASSET

Every headline quantity carries an **evidence class** — DERIVED RECOMPUTED MEASURED REQUIREMENT — and, where a number is a modelled extrapolation rather than a demonstrated value, it is labelled as such and its downside is shown next to it. Several quantities in the underlying corpus moved after first publication; where a value has been withdrawn or restated, the record says so plainly. This is deliberate: a diligence team will find the load-bearing assumptions, so the document surfaces them first.

TWO EDITIONS

This volume is issued in two editions. The **public edition** (light) carries the physics and the design only — no dollar, price, or per-kilogram figure appears anywhere in it. The **internal edition** (dark) adds the economics, the funding architecture, and the defense-commercial analysis, and is marked *Confidential* accordingly; it is not for public distribution. Where the commercial case rests on a modelled assumption rather than a demonstrated one, it is labelled as such and its downside is shown alongside it, on the same terms as the physics.

TITLE	The Kronos Fleet — Hyperion · Aegis · MetroVolt: A Combined Design & Commercialization Study
AUTHOR	Priyanca Ford, Founder & CEO, on behalf of Kronos Fusion Energy
EDITION	2026 Combined Editorial · first issue
COMPANION WORKS	The five-paper arXiv drop — (1) Breeder, (2) Burner, (3) REBCO magnet & tape, (4) Direct Energy Conversion, (5) AI/ML/Quantum control — with matching numbered Zenodo deposits, plus the IOP journal and IAEA-FEC submissions. Patents were filed before the drop.
NAMING	Hyperion = the breeder; Aegis (defense) and MetroVolt (data-center) = one generator in two housings. Internal mode letters (D1, L) do not appear on public surfaces.
STATUS	Conceptual design & simulation study. Nothing herein is a construction commitment.

HOW TO READ THIS VOLUME

The fleet at a glance, and the way its numbers are marked

This volume opens with *Orientation*, presents the five research papers as a bound sequence, and closes with the *Apparatus*. *Foundations* sets out the three general results both machines rest on. *Paper One* is the Hyperion breeder; *Paper Two* the Aegis / MetroVolt generator; *Papers Three, Four and Five* are the enabling science — high-field REBCO magnets and tape, direct energy conversion, and the AI / ML / quantum control stack. A *Digital Twin & 3-D Model* part follows, then the *Environmental* profile. The *Economics* and levelized cost and the *Business Case* and diligence record appear in the internal edition only; the *Simulations* proof record and the Apparatus — patent portfolio, team, limitations, and sources — close both editions.

THE FLEET AT A GLANCE

	HYPERION	AEGIS	METROVOLT
Role	Strategic-isotope foundry	Defense installation power	Campus power
Machine	**Spherical tokamak**	**Tandem mirror**	**Tandem mirror**
Fuel	Deuterium–tritium	Deuterium–helium-3	Deuterium–helium-3
Delivers	Tritium · ^{3}He · 14 MeV n	Resilient installation power	Firm campus power
Physics bar	**Fusion gain only**	Closure (gates named)	Closure + lunar ^{3}He
In the fleet	Breeds the fuel	Proves the generator	Commercial destination

HOW THE NUMBERS ARE MARKED

Every headline quantity carries an evidence class — DERIVED from first principles, RECOMPUTED from raw data, MEASURED in hardware, or a REQUIREMENT yet to be met. Financial figures carry a case label and are confined to the internal (confidential) edition. Values that moved after first publication are shown as withdrawn or restated rather than quietly changed. A capability you can evaluate is one whose limits are on the page.

ABSTRACT

Free-Boundary Equilibrium and Ideal-MHD Stability of a Compact Spherical-Tokamak Breeder: Troyon, Mercier, Ballooning and External-Kink Margins with a Vertical-Stability Flag

A fusion design point is physical only if it corresponds to a self-consistent free-boundary equilibrium that is stable to the fast ideal-magnetohydrodynamic (MHD) modes. We construct the equilibrium of the frozen compact negative-triangularity spherical-tokamak (ST) breeder and test its ideal stability on a reproducible, GPU-accelerated computational chain. A free-boundary Grad–Shafranov solution reproduces the design point ($I_p = 9.66$ MA, $B_0 = 8.0$ T, $R_0 = 1.20$ m, aspect ratio $A = 2.5$, triangularity $\delta = -0.30$) with a poloidal beta $\beta_p = 0.371$, edge safety factor $q_{95} = 2.90$, internal inductance $\ell_i = 1.40$, and a normalized beta $\beta_N = 2.13$. Against a no-wall Troyon pressure limit of $\beta_N \approx 3.5$ the operating point carries a factor 1.64 of margin; the more restrictive no-wall external-kink limit ($\beta_N \approx 2.8$), evaluated over the range $\beta_N = 2.13$–2.44, leaves a binding margin of 1.15–$1.31\times$. The equilibrium is Mercier-stable and s–α ballooning-stable on every confinement surface with $q > 1$ (a small $q < 1$ core pocket carries only the benign sawtooth), and a formal Richardson grid-convergence study on $129/257/513$ meshes places the equilibrium metrics at an observed order of accuracy $p = 0.89$ with a fine-grid convergence index of 0.10%. We formalize the governing equations—Grad–Shafranov force balance, the ideal energy principle, the Mercier and ballooning local criteria, the Troyon and resistive-wall external-kink limits, and the axisymmetric vertical mode—as explicit mathematics, and we resolve the vertical-stability question the free-boundary elongation ($\kappa = 2.47$) raises: the open-loop growth is $\gamma\tau_w = 8.05$ at the nominal $\kappa = 2.0$, diverging only at $\kappa_c \approx 2.8$, and a proportional–derivative controller with a stabilizing gain $K_p > 3.03 \times 10^4\ \mathrm{V\,m^{-1}}$ arrests a seed displacement within 3.5 ms against a 1.5 ms open-loop growth time. One honest gate is carried forward: a full resistive-wall $n = 1$ energy-principle eigenvalue solve (DCON/MARS) still owes the reduced kink metric its final confirmation. Within that clearly stated envelope, the frozen design point is a consistent, controllable, ideal-MHD-stable equilibrium.

Open-access deposit (code & data, CC BY 4.0): DOI 10.5281/zenodo.22645740 · Zenodo community *kronos_fusion_energy*. Explore it live: interactive 3-D model · physics validator.

Keywords: free-boundary equilibrium · Grad--Shafranov · ideal MHD · Mercier criterion · ballooning modes · external kink · Troyon limit · vertical stability · negative triangularity · spherical tokamak

CONTENTS

Table of Contents

NOMENCLATURE

Symbols, units, and the names of things

Q	plasma (fusion) gain, P_{fus}/P_{aux}
Q_E	engineering gain, net electric out / recirculating in
H_{98}	confinement enhancement over the IPB98(y,2) scaling
Z_{eff}	effective ion charge
c_{ee}	electron–electron bremsstrahlung leading coefficient, 2.120022 (exact)
τ_E	energy confinement time
I_p	plasma current
R_0, a	major radius, minor radius
κ, δ	elongation, triangularity
β_N	normalized plasma beta (Troyon-normalized)
TBR	tritium breeding ratio
DEC	direct energy conversion
CF	plant capacity factor (availability)
FOAK / NOAK / BOAK	first / n^{th} / best of a kind
Hyperion	the ST breeder (internal: Mode D2)
Aegis	the generator, defense/installation housing (internal: Mode M)
MetroVolt	the generator, data-center housing (Mode M)

free-boundary equilibrium; Grad–Shafranov; ideal MHD; Mercier criterion; ballooning modes; external kink; Troyon limit; vertical stability; negative triangularity; spherical tokamak

§ 1

Introduction

WHY EQUILIBRIUM AND IDEAL STABILITY COME FIRST

Every downstream result in a fusion reactor design—confinement, neutronics, tritium breeding, magnet loads—rests on the assumption that the machine can hold a plasma at all. That assumption is quantitative and testable: the operating point must correspond to a self-consistent solution of the Grad–Shafranov equation with the design currents and boundary shape, and that equilibrium must lie inside the stability boundaries of ideal magnetohydrodynamics, the fastest and most violent instabilities available to the plasma [1,2]. An ideal-MHD-unstable equilibrium grows on the Alfv\'en time, of order microseconds, and no control system can recover it; the design is therefore obligated to demonstrate a quantified margin against the pressure-driven and current-driven ideal limits before any transport or nuclear claim can be trusted.

The Kronos Hyperion breeder is a compact, high-current spherical tokamak: it holds $I_p = 9.66$ MA at a major radius of only $R_0 = 1.20$ m and aspect ratio $A = 2.5$, behind a demountable centrepost magnet at a peak field of 16.84 T, in a negative-triangularity ($\delta = -0.30$) configuration. Two features of this design point put ideal stability squarely on the critical path. First, the low aspect ratio and high current place the machine in a regime where the Troyon and external-kink limits are set by the ratio $I_p/(aB_0)$ and must be evaluated for the actual, strongly shaped boundary rather than a circular idealization [3,4,5]. Second, the strong shaping needed to reach good confinement produces a highly elongated cross-section, and elongation directly excites the axisymmetric ($n = 0$) vertical instability, which in a compact ST grows on a millisecond timescale and must be actively stabilized. Both questions are answered here, with the mathematics made explicit and every headline number traced to a frozen anchor in the Kronos Physics De-Risking Register [26].

NEGATIVE TRIANGULARITY AND THE COMPACT-ST CONTEXT

Negative triangularity (NT) is chosen for the breeder because it accesses good core confinement without an H-mode edge pressure pedestal and hence without the edge-localized-mode (ELM) cycle of conventional operation, as established on DIII-D [6] and reviewed comprehensively by Marinoni, Sauter and Coda [7]. The quiet, ELM-free NT edge is an operational asset, but it is only an asset if the underlying global equilibrium is itself stable to the ideal modes; the pedestal-avoidance argument speaks to the transient edge loads, not to the volume-averaged pressure limit or the current-driven kink. The compact-ST design tradition—from the spherical-tokamak pilot-plant studies of Menard *et al.* [3] to compact high-field concepts such as ARC [4] and SPARC [5]—has repeatedly shown that low aspect ratio buys high β and high current density at the cost of demanding vertical control and a narrow window between the no-wall and ideal-wall kink limits. The spherical-torus experiment NSTX, in particular, routinely operated above its no-wall limit with resistive-wall-mode (RWM) stabilization by rotation and feedback [8], which frames both the opportunity and the obligation for a compact ST breeder.

PRIOR ART IN EQUILIBRIUM AND IDEAL-MHD COMPUTATION

The tools used here descend from a mature computational lineage. Free-boundary Grad–Shafranov reconstruction and design date to the EFIT family [9]; modern open solvers—FreeGS [10] and its dynamic successor FreeGSNKE [11], the Hermite finite-element code CHEASE [12], and the local Miller equilibrium parametrization [13]—make the equilibrium reproducible. Global pressure limits are organized by the Troyon normalization [14]; local interchange stability by the Mercier criterion [15] in the Glasser–Greene–Johnson form implemented in DCON [18]; high-mode-number pressure-driven modes by the ballooning representation of Connor, Hastie and Taylor [17]; the ideal energy principle itself by the Newcomb formulation [16]. Extended-MHD dynamics—disruption and nonlinear stability—are computed directly in NIMROD [19]. The vertical mode and its stabilization are governed by the resistive-wall physics of Bondeson and Ward [20], the stability-margin framework of Portone [21], and the elongation-limit theory of Freidberg, Cerfon and Lee [22]. What a design paper owes, beyond citing these tools, is a single self-consistent application of them to a specific, frozen operating point with quantified margins and a formal convergence audit—which is what we provide.

CONTRIBUTION

This paper (i) states the governing equations of the free-boundary equilibrium and of each ideal-MHD limit as explicit mathematics (§2); (ii) documents the GPU-accelerated computational methodology, including a formal Richardson grid-convergence index and the reference-code chain, with no invented data drawn as a result (§3); (iii) reports the converged equilibrium and its margins against the Troyon, Mercier, ballooning and external-kink limits (§4); and (iv) resolves the vertical-stability question the elongation raises, deriving the open-loop growth-rate scaling with elongation and the closed-loop control authority that arrests it. We compare each result quantitatively to the published spherical-torus and compact-tokamak literature (§5) and carry forward, openly, the one item the reduced kink metric leaves for a full energy-principle solve (§6). Throughout, we cite companion papers in the Kronos series that supply the confinement basis, the coil set, and the disruption consequence of the boundaries mapped here.

§ 2

Governing equations and the formal problem

IDEAL-MHD FORCE BALANCE AND THE GRAD–SHAFRANOV EQUATION

The plasma is described by the ideal-MHD equilibrium equations,

$$J \times B = \nabla p, \qquad \nabla \times B = \mu_0 J, \qquad \nabla \cdot B = 0,$$

which state that the Lorentz force balances the pressure gradient and that the field is solenoidal and current-carrying. Axisymmetry ($\partial/\partial\phi = 0$ in cylindrical coordinates (R, ϕ, Z)) permits the representation of the magnetic field in terms of the poloidal flux function $\psi(R, Z)$ and the poloidal-current function $F(\psi) = RB_\phi$,

$$B = \frac{1}{R}\nabla\psi \times \hat{e}_\phi + \frac{F(\psi)}{R}\hat{e}_\phi.$$

Equation (1) then reduces to the Grad–Shafranov equation for ψ [2,1],

$$\Delta^*\psi \equiv R\frac{\partial}{\partial R}\left(\frac{1}{R}\frac{\partial\psi}{\partial R}\right) + \frac{\partial^2\psi}{\partial Z^2} = -\mu_0 R^2\frac{\mathrm{d}p}{\mathrm{d}\psi} - F\frac{\mathrm{d}F}{\mathrm{d}\psi},$$

a quasilinear elliptic partial differential equation in which the two free-profile functions $p(\psi)$ and $F(\psi)$ close the system. The toroidal current density that appears as the source is

$$J_\phi(R, \psi) = R\frac{\mathrm{d}p}{\mathrm{d}\psi} + \frac{1}{\mu_0 R}F\frac{\mathrm{d}F}{\mathrm{d}\psi}.$$

Equation (3) is the field the whole design must satisfy; every quantity below is a functional of its solution.

THE FREE-BOUNDARY PROBLEM

In a real device the plasma boundary is not prescribed; it is determined self-consistently by the balance between the plasma current and the currents in the external poloidal-field (PF) coils. The free-boundary problem couples the Grad–Shafranov equation (3) in the plasma region Ω_p to the vacuum region carrying discrete coil currents I_k at positions (R_k, Z_k). Writing the total flux as the superposition of the plasma and coil contributions through the toroidal Green's function $G(R, Z; R', Z')$,

$$\psi(R, Z) = \int_{\Omega_p} G(R, Z; R', Z')\, J_\phi(R', Z')\,\mathrm{d}R'\mathrm{d}Z' + \sum_k G(R, Z; R_k, Z_k)\, I_k,$$

the plasma boundary is the outermost closed flux surface (the last closed flux surface, LCFS), either limited or bounded by an X-point where $\nabla\psi = 0$. The Green's function for the elliptic operator Δ^* is known in closed form in terms of complete elliptic integrals [9,10], so equation (5) removes the outer boundary condition to infinity and reduces the free-boundary problem to a fixed-point iteration on the coil currents that realize the target shape (§3). The Hyperion equilibrium is solenoid-free: the ohmic central solenoid of a conventional tokamak is absent, and the flux state is carried by the PF set and the bootstrap-aligned current profile.

GLOBAL EQUILIBRIUM METRICS

The safety factor—the pitch of the field lines, and the central organizing quantity of tokamak stability—is the flux-surface functional

$$q(\psi) = \frac{1}{2\pi}\oint_{\psi=\mathrm{const}} \frac{F(\psi)}{R\,|\nabla\psi|}\,\mathrm{d}\ell_p,$$

with q_{95} its value on the surface enclosing 95% of the poloidal flux. The volume-averaged plasma pressure is normalized to the magnetic pressure through the several beta parameters,

$$\beta_t = \frac{\langle p\rangle}{B_0^2/2\mu_0}, \qquad \beta_p = \frac{2\mu_0\langle p\rangle}{\langle B_\theta^2\rangle}, \qquad \beta_N = \frac{\beta_t[\%]}{I_p[\mathrm{MA}]/(a[\mathrm{m}]\,B_0[\mathrm{T}])},$$

where β_t is the toroidal, β_p the poloidal beta, $a = R_0/A$ the minor radius, and β_N the Troyon-normalized beta that collapses the pressure limit onto a near-universal number. The current distribution is characterized by the internal inductance per unit length,

$$\ell_i = \frac{\langle B_\theta^2\rangle_V}{\langle B_\theta\rangle_{\partial\Omega}^2} = \frac{2}{\mu_0^2 I_p^2 R_0}\int_V B_\theta^2\,\mathrm{d}V,$$

which measures the peaking of the current profile and enters the vertical-stability and kink problems directly. The converged values of q_{95}, β_p, ℓ_i and β_N are the equilibrium fingerprints reported in §4.

THE IDEAL-MHD ENERGY PRINCIPLE

Stability is decided by the sign of the change in potential energy under a displacement field $\xi(r)$. For a static ideal equilibrium the linearized equation of motion is self-adjoint, and the plasma is stable if and only if the energy functional

$$\delta W[\xi, \xi] = \delta W_F + \delta W_S + \delta W_V \;\geq\; 0$$

for all admissible ξ, where δW_F, δW_S and δW_V are the fluid, surface and vacuum contributions [1,16]. The fluid term, written in the standard form that separates the stabilizing from the potentially destabilizing physics, is

$$\delta W_F = \frac{1}{2}\int_{\Omega_p}\left[\underbrace{\frac{|Q_\perp|^2}{\mu_0}}_{\text{field-line bending}} + \underbrace{\frac{B^2}{\mu_0}\left|\nabla\cdot\xi_\perp + 2\xi_\perp\cdot\kappa\right|^2}_{\text{magnetic compression}} + \underbrace{\gamma p\,|\nabla\cdot\xi|^2}_{\text{plasma compression}} - \underbrace{2(\xi_\perp\cdot\nabla p)(\kappa\cdot\xi_\perp^*)}_{\text{interchange/ballooning}} - \underbrace{j_\parallel(\xi_\perp^*\times\hat{b})\cdot Q_\perp}_{\text{current-driven kink}}\right]\mathrm{d}V,$$

with $Q = \nabla\times(\xi\times B)$ the perturbed magnetic field, $\kappa = (\hat{b}\cdot\nabla)\hat{b}$ the field-line curvature, $\hat{b} = B/B$, and $j_\parallel$ the parallel current density. The first three terms are positive-definite: they are the energy cost of bending and compressing field lines and of compressing the plasma, and they set the stabilizing floor. The last two terms can be negative and are the two independent drives of ideal instability—the pressure gradient acting against unfavourable curvature (interchange and its ballooning localization) and the parallel current (the kink). Minimizing (10) over the perpendicular displacement, and then over the toroidal mode number n, yields the stability boundaries evaluated below. The three limits—Mercier (local, $n\to\infty$ interchange), ballooning (high-n, field-aligned), and the low-n external kink/Troyon (global)—are the successive minimizations of the same functional.

THE INTERCHANGE (MERCIER) CRITERION

The most localized minimizer of (9) is the interchange, a displacement concentrated near a single rational surface. Following Mercier [15] in the Glasser–Greene–Johnson representation used by DCON [18], ideal interchange stability on a flux surface requires the Mercier index to satisfy

$$D_M \equiv E + F + H^2 \;<\; \frac{1}{4}, \qquad \text{equivalently} \qquad D_I \equiv \frac{1}{4} - D_M \;>\; 0,$$

where the surface functionals E, F and H collect, respectively, the pressure-curvature interchange drive, the average favourable-curvature (Pfirsch–Schl\"uter) restoring term, and the shear–interchange cross coupling. In the physically transparent limit, equation (11) balances the destabilizing pressure gradient against the product of the magnetic shear $s = (r/q)\,\mathrm{d}q/\mathrm{d}r$ and the average magnetic well; strong shear and a favourable average well stabilize, and the criterion is the necessary local condition every confinement surface must clear. We report the margin D_I of equation (11) across the profile (figure 4, left).

HIGH-MODE-NUMBER BALLOONING MODES

Between the local interchange and the global kink lies the ballooning mode: a high-toroidal-number, field-aligned displacement that balloons on the outboard, unfavourable-curvature side. In the ballooning representation of Connor, Hastie and Taylor [17], the two-dimensional eigenvalue problem collapses to a one-dimensional ordinary differential equation along a field line, parametrized by the extended poloidal angle θ,

$$\frac{\mathrm{d}}{\mathrm{d}\theta}\left[(1+\Lambda^2)\,\frac{\mathrm{d}\hat{\xi}}{\mathrm{d}\theta}\right] + \alpha\big[\cos\theta + (s\theta - \alpha\sin\theta)\sin\theta\big]\hat{\xi} = 0, \qquad \Lambda = s\theta - \alpha\sin\theta,$$

where s is the local magnetic shear and

$$\alpha = -\frac{2\mu_0 q^2 R_0}{B_0^2}\,\frac{\mathrm{d}p}{\mathrm{d}r}$$

is the normalized pressure gradient. Marginal stability—the existence of a bounded, non-trivial solution of equation (12)—traces the first-stability boundary in the s–α plane; the equilibrium is ballooning-stable on a surface if its operating (s, α) lies below that boundary (figure 5). Negative triangularity is favourable here because it reshapes the local magnetic geometry to keep α modest at finite shear, an effect we quantify against the companion edge-stability analysis [doi:10.5281/zenodo.22645949].

THE EXTERNAL KINK AND THE TROYON LIMIT

The lowest-n minimizers of (9), the external kink modes, are driven by the parallel current and the edge pressure gradient and are held off by keeping the edge safety factor above the resonant value and by the proximity of a conducting wall. Collapsing the global pressure limit onto a single number, Troyon [14] showed that the maximum stable toroidal beta scales as

$$\beta_t^{\max}[\%] = g_T \frac{I_p[\mathrm{MA}]}{a[\mathrm{m}]\, B_0[\mathrm{T}]}, \qquad \Longleftrightarrow \qquad \beta_N^{\max} = g_T,$$

with the Troyon coefficient g_T of order unity; the no-wall ideal limit sits near $g_T \approx 2.8$ for the current-driven external kink and near $g_T \approx 3.5$ for the pressure-driven global mode, depending on profiles and shape. Above the no-wall limit but below the ideal-wall limit, the external kink becomes a resistive-wall mode (RWM) that grows on the slow wall time and can be stabilized by rotation and feedback [20,8]; its growth rate obeys the resistive-wall dispersion

$$\gamma\tau_w = \frac{c_{\mathrm{nw}} - \beta_N}{\beta_N - c_{\mathrm{iw}}},$$

where c_{nw} and c_{iw} are the no-wall and ideal-wall marginal β_N and τ_w is the wall resistive time. We evaluate the kink margin as the ratio of the no-wall limit to the operating β_N and report it as the binding global metric, while stating clearly (§6) that equation (15) with a realistic conducting structure is the full calculation the reduced metric still owes.

THE AXISYMMETRIC VERTICAL MODE

Elongation is the price of confinement: shaping the plasma to $\kappa > 1$ improves current-carrying capacity and stability against the pressure-driven modes, but it renders the equilibrium unstable to the $n = 0$ axisymmetric vertical displacement. A rigid vertical shift ξ_Z of an elongated plasma in the externally imposed field experiences a destabilizing force proportional to the field decay index $n_{\mathrm{dec}} = -(R/B_Z)\,\partial B_Z/\partial R$; when $n_{\mathrm{dec}} < 0$, as it must be to elongate the plasma, the force is restoring against the wall but destabilizing in vacuum, and the plasma runs away vertically. A perfectly conducting wall at finite distance stabilizes the mode ideally; a resistive wall reduces the growth to the wall timescale. Modelling the plasma as a massless rigid current filament coupled to a resistive wall of time τ_w, the vertical dispersion relation reduces to

$$\gamma\tau_w = \frac{f}{1-f}, \qquad f \equiv \frac{n_{\mathrm{dec}}^{\mathrm{plasma}}}{n_{\mathrm{dec}}^{\mathrm{iw}}},$$

where f is the ratio of the destabilizing field index to its ideal-wall marginal value and $m_s \equiv 1 - f$ is the Portone stability margin [21]. Equation (16) makes the elongation dependence explicit: as κ rises toward the critical κ_c at which $f \to 1$ (the ideal-wall limit), $\gamma\tau_w$ diverges and no passive or feedback scheme can help. Below κ_c the mode grows on the wall time and is stabilizable. Active stabilization is provided by a control coil driven by a proportional–derivative (PD) law on the measured vertical position,

$$V_{\mathrm{coil}}(t) = K_p\, Z(t) + K_d\, \dot{Z}(t),$$

and closed-loop stability requires the roots of the characteristic polynomial obtained by inserting (17) into the coupled plasma–wall–coil circuit equations to lie in the left half-plane—a condition that reduces, for the dominant unstable pole, to a threshold on the proportional gain K_p. The maximum feedback-accessible elongation is then set not by κ_c itself but by the achievable controller gain and power, the trade quantified by Freidberg, Cerfon and Lee [22] and evaluated for Hyperion in §4 and in the companion vertical-stability paper [doi:10.5281/zenodo.22645834].

§ 3

Computational methodology: the GPU-HPC campaign

OVERVIEW AND REPRODUCIBILITY CONTRACT

Every number in §4 is produced by a fixed chain of open, version-pinned solvers run on the NVIDIA GPU HPC campaign and cross-checked on the in-house verification node; each is a frozen anchor in the de-risking register [26] with a serial identifier cited inline, and each is regenerable from the archived inputs and the figure-generation script deposited with this paper. No result depends on proprietary data. The chain has four stages: (1) the free-boundary Grad–Shafranov solve; (2) a formal Richardson grid-convergence audit; (3) the local ideal-stability metrics (Mercier and ballooning) evaluated surface-by-surface on the converged equilibrium; and (4) the extended-MHD arbiter and the vertical-control model. Figure 1 shows the chain and the serial for each stage.

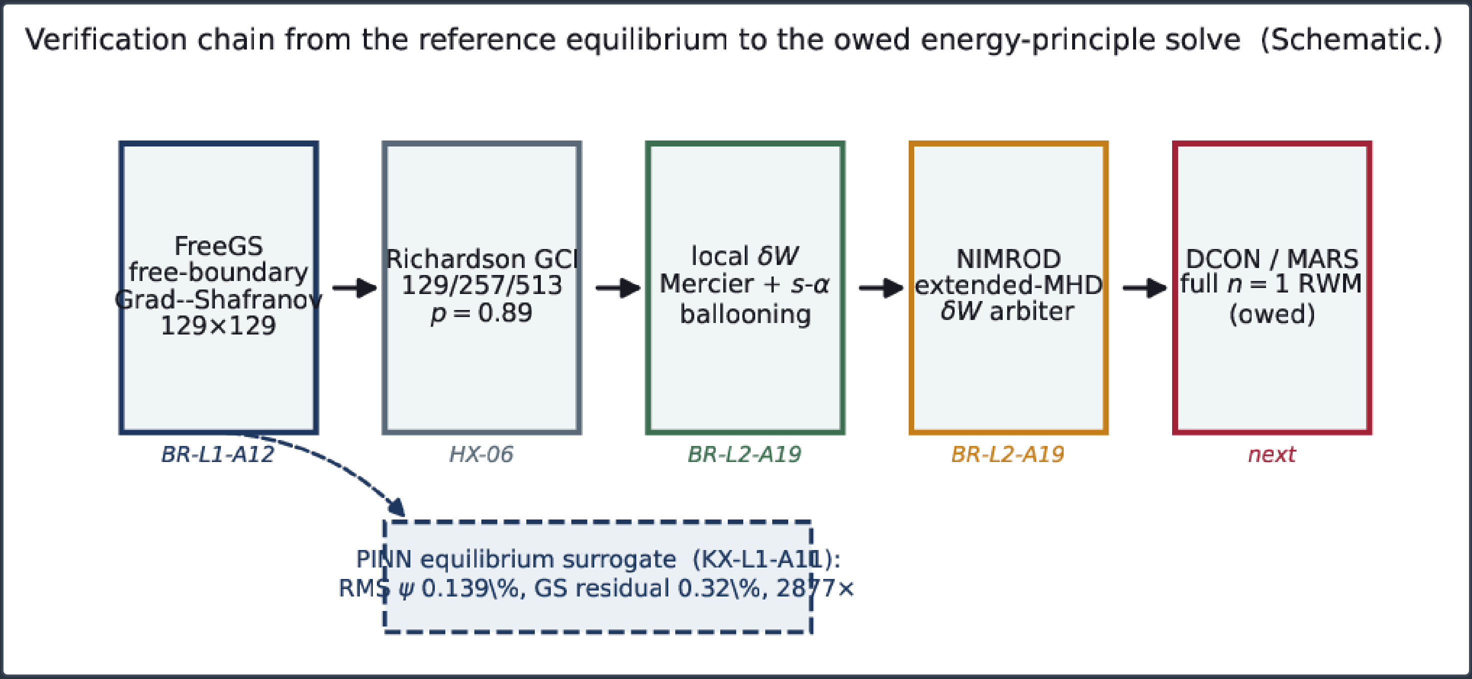

(Schematic.) The verification chain from the reference free-boundary equilibrium to the owed full energy-principle solve. FreeGS (BR-L1-A12) supplies the converged equilibrium; a Richardson grid-convergence audit (HX-06) certifies mesh independence; the local δW metrics (Mercier and s–α ballooning, BR-L2-A19) and the NIMROD extended-MHD arbiter test stability; a full $n = 1$ resistive-wall eigenvalue solve (DCON/MARS) is the owed next step. A physics-informed neural surrogate (KX-L1-A11) reproduces the equilibrium at kilohertz rates for the control loop. Serials refer to the register [26].

FREE-BOUNDARY GRAD–SHAFRANOV SOLVER

The reference equilibrium is computed with FreeGS [10], a free-boundary Grad–Shafranov solver, on a 129×129 (R, Z) mesh spanning the vessel. The elliptic operator Δ^* of equation (3) is discretized by second-order centred finite differences,

$$(\Delta^*\psi)_{i,j} = \frac{\psi_{i+1,j} - 2\psi_{i,j} + \psi_{i-1,j}}{(\Delta R)^2} - \frac{1}{R_i}\frac{\psi_{i+1,j} - \psi_{i-1,j}}{2\Delta R} + \frac{\psi_{i,j+1} - 2\psi_{i,j} + \psi_{i,j-1}}{(\Delta Z)^2},$$

and the nonlinear source is resolved by Picard iteration: given the current iterate $\psi^{(m)}$, the profiles $p'(\psi)$ and $FF'(\psi)$—parametrized to hit the target I_p, β_p and boundary shape—set the toroidal current (4), the interior solve inverts the discretized Δ^*, and the vacuum flux from the coil currents is added through the Green's-function form (5). The boundary flux on the computational domain is supplied by the free-boundary Green's-function integral so that no artificial outer wall is imposed. The iteration is accelerated by under-relaxation, $\psi^{(m+1)} = (1-\omega)\psi^{(m)} + \omega\,\tilde{\psi}$, and converged to a relative flux residual

$$\frac{\left\|\psi^{(m+1)} - \psi^{(m)}\right\|_2}{\left\|\psi^{(m+1)}\right\|_2} < 10^{-8},$$

at which point the coil currents that realize the target LCFS shape (κ, δ, X-point locations) have been found by a constrained least-squares fit. The converged solution reproduces the design point at $I_p = 9.66\,\mathrm{MA}$, $B_0 = 8.0\,\mathrm{T}$, and $\delta = -0.334$ in the free-boundary solution (against the nominal -0.30), and is the ground truth for everything downstream (BR-L1-A12).

FORMAL MESH INDEPENDENCE: THE GRID-CONVERGENCE INDEX

A design-grade equilibrium claim must be shown to be mesh-independent, not merely converged on one grid. We apply the Richardson-extrapolation grid-convergence index (GCI) of Roache [23] across three systematically refined meshes, 129×129, 257×257 and 513×513, with constant refinement ratio $r = 2$ (HX-06). For an integral equilibrium metric f (plasma volume, β_N), the observed order of accuracy is

$$p = \frac{1}{\ln r} \ln\left(\frac{f_1 - f_2}{f_2 - f_3}\right),$$

with f_1, f_2, f_3 the coarse-to-fine values, and the fine-grid convergence index is

$$\mathrm{GCI}_{\text{fine}} = F_s \frac{|f_3 - f_2|/|f_3|}{r^p - 1}, \qquad F_s = 1.25.$$

The Richardson-extrapolated continuum value is $f_{\text{ext}} = f_3 + (f_3 - f_2)/(r^p - 1)$. The audit returns an observed order $p = 0.89$, a fine-grid $\mathrm{GCI} = 0.10\%$, and total mesh sensitivity below 0.4% (figure 6)—so the equilibrium metrics are certified mesh-independent to sub-percent, closing the register's formal-convergence item.

LOCAL IDEAL-STABILITY METRICS

On the converged, mesh-independent equilibrium, the Mercier index (11) and the ballooning eigenproblem (12) are evaluated surface-by-surface across the normalized poloidal flux ψ_N (BR-L2-A19). The Mercier functionals E, F, H are computed from the flux-surface-averaged geometry of the solution; the ballooning ODE is integrated along field lines with the local $s(\psi_N)$ and $\alpha(\psi_N)$ read from the equilibrium, and marginality is detected by the sign of the least eigenvalue. Both are $O(N^2)$ per surface and run in seconds on the verification node once the equilibrium is in hand.

EXTENDED-MHD ARBITER AND THE OWED $n = 1$

n=1 solve Beyond the local metrics, the disruption and nonlinear-stability arbiter is the reference 3-D extended-MHD code NIMROD [19], run directly—not as a surrogate—on owned HPC; it confirms free-boundary MHD stability at the design point and supplies the nonlinear disruption pathway analyzed in the companion disruption paper [doi:10.5281/zenodo.22645724]. The one calculation the present reduced assessment does not perform is the full low-n resistive-wall energy-principle eigenvalue solve—the DCON [18]/MARS class of code that returns the RWM growth rate of equation (15) with a realistic conducting structure. We report the kink margin as a reduced metric and name the owed solve explicitly (§6).

PHYSICS-INFORMED SURROGATE AND THE NVIDIA GPU HPC CAMPAIGN

The reference solves above are the design authority; the control loop needs the same equilibrium at kilohertz rates. A physics-informed neural network (PINN) is trained to reproduce the FreeGS ground truth, with the Grad–Shafranov operator of equation (3) enforced as a residual loss at collocation points (KX-L1-A11). Against the free-boundary solver the surrogate reaches an RMS flux error of 0.139% and a Grad–Shafranov operator residual of 0.32% at a $2877\times$ speed-up, so the equilibrium is available inside the real-time cycle without loss of fidelity; the sub-millisecond neural equilibrium reconstruction is developed in the companion paper [doi:10.5281/zenodo.22645801]. Training of the surrogate, the multi-grid convergence sweeps, and the elongation and β scans of §4 were executed on the NVIDIA GPU HPC campaign (a mixed A100/H100/A10 fleet), with the reference equilibrium and extended-MHD solves cross-checked on the in-house verification node so that the fast surrogate is always audited against the frozen reference. The campaign provides the throughput to treat the stability boundaries as scans rather than single points, and the verification node guarantees that no surrogate result enters the design record without a reference-code check.

§ 4

Results

THE CONVERGED EQUILIBRIUM

The free-boundary solve reproduces the frozen design point as a consistent equilibrium. Table 1 collects the converged parameters; figure 2 shows the flux-surface geometry, with the negative-triangularity LCFS, the outboard-shifted magnetic axis, and the inboard centrepost that carries the $16.84\,\mathrm{T}$ toroidal field. Figure 2 shows the safety-factor and pressure profiles consistent with the converged solution: q rises monotonically from a shallow $q_0 < 1$ core (the benign sawtooth pocket) to $q_{95} = 2.90$, and the pressure profile carries the $\beta_p = 0.371$, $\ell_i = 1.40$ current peaking.

QUANTITY	VALUE	BASIS
plasma current I_p	$9.66\,\mathrm{MA}$	design anchor
toroidal field B_0	$8.0\,\mathrm{T}$	design anchor
major radius R_0	$1.20\,\mathrm{m}$	design anchor
aspect ratio A	2.5	design anchor
triangularity δ (nominal)	-0.30	design anchor
triangularity δ (free-boundary)	-0.334	FreeGS solve
poloidal beta β_p	0.371	FreeGS solve
edge safety factor q_{95}	2.90	FreeGS solve
internal inductance ℓ_i	1.40	FreeGS solve
normalized beta β_N	2.13	FreeGS solve
elongation κ (free-boundary, flagged)	2.47	FreeGS solve

Free-boundary equilibrium parameters at the frozen design point (BR-L1-A12). Canonical anchors are Tier-2 frozen; the free-boundary elongation is the value reached by the solve at the target shape.

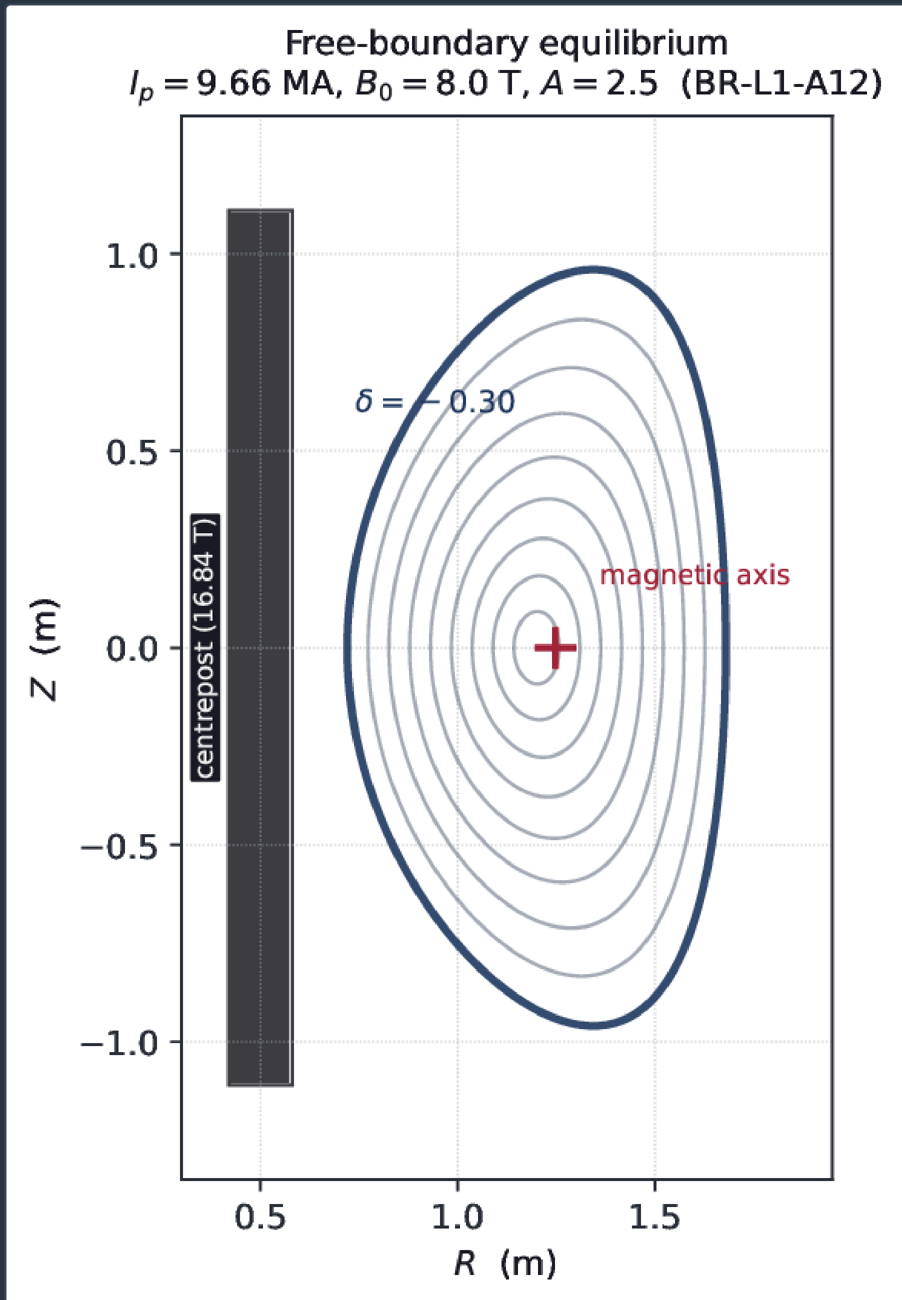
Free-boundary equilibrium
$I_p = 9.66$ MA, $B_0 = 8.0$ T, $A = 2.5$ (BR-L1-A12)
$\delta = -0.30$
magnetic axis
centrepost (16.84 T)
Z (m)
R (m)
1.0
0.5
0.0
−0.5
−1.0
0.5
1.0
1.5

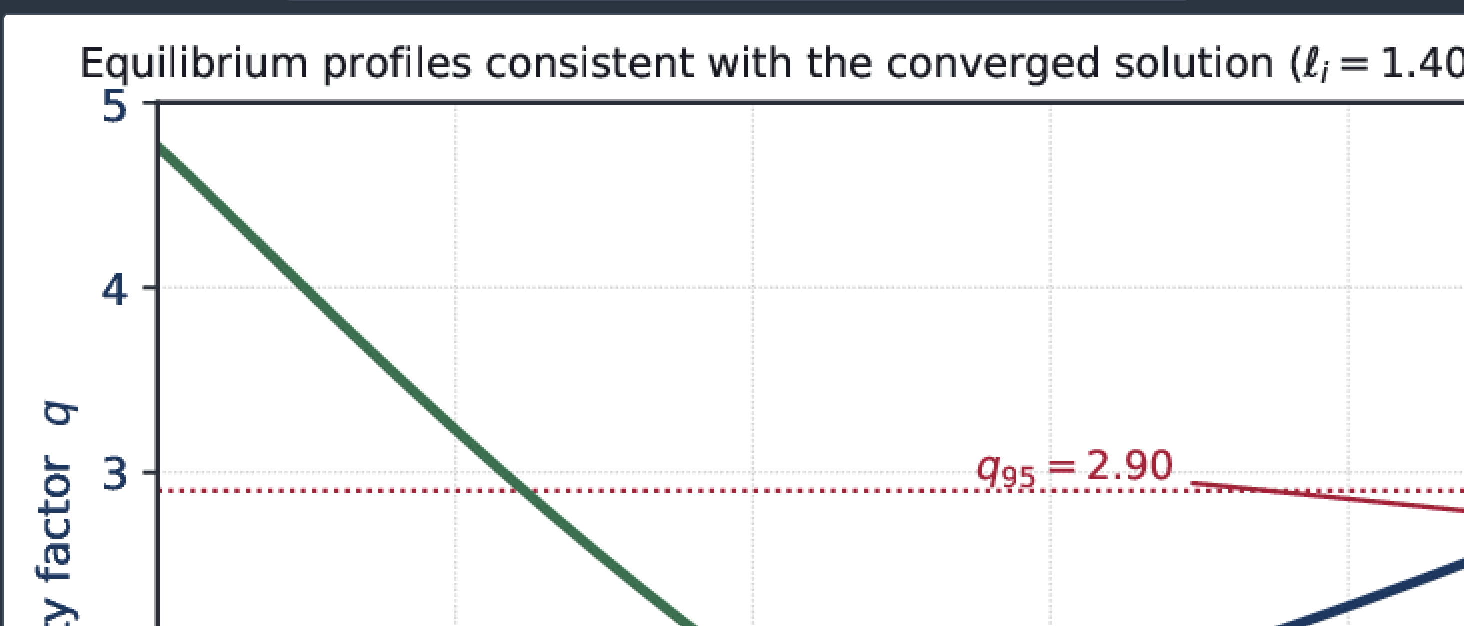
Equilibrium profiles consistent with the converged solution ($\ell_i = 1.40$
$q_{95} = 2.90$
ty factor q
5
4
3

GLOBAL BETA AND THE TROYON MARGIN

The normalized beta of the operating point is $\beta_N = \mathbf{2.13}$. Against the no-wall Troyon pressure limit of $\beta_N \approx \mathbf{3.5}$, equation (14), the design carries a factor **1.64** of margin and operates comfortably below the global pressure boundary (figure 3). An independent robustness check confirms that this headroom is not fragile: a 40,000-sample Monte-Carlo propagation of realistic input uncertainty returns an ensemble-mean $\beta_N = \mathbf{1.53}$ (FREEZE-CONF), i.e. the central tendency of the design distribution sits even further below the limit than the nominal operating point, so the pressure-limit margin is robust to input uncertainty rather than a knife-edge.

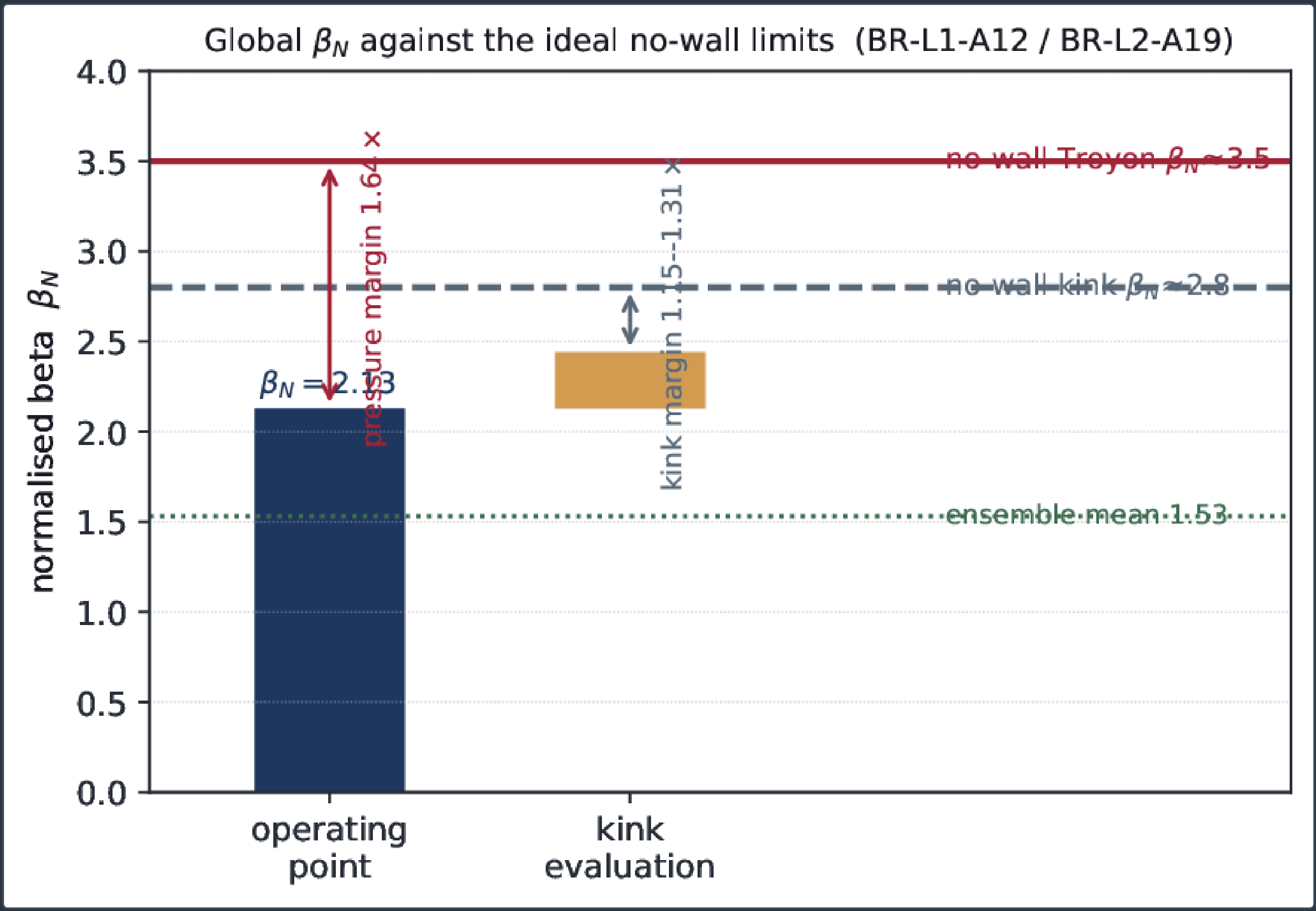

Global β_N against the ideal no-wall limits (BR-L1-A12 / BR-L2-A19). The operating point ($\beta_N = \mathbf{2.13}$) carries a factor **1.64** of margin against the no-wall Troyon pressure limit ($\approx \mathbf{3.5}$); the more restrictive external-kink no-wall limit ($\approx \mathbf{2.8}$), evaluated over the band $\beta_N = \mathbf{2.13}$–$\mathbf{2.44}$, leaves the binding margin of $\mathbf{1.15}$–$\mathbf{1.31}\times$. The dotted line is the 40,000-sample ensemble mean.

LOCAL IDEAL STABILITY: MERCIER AND BALLOONING

Evaluated surface-by-surface on the converged equilibrium, the Mercier margin $D_I = \frac{1}{4} - D_M$ of equation (11) is positive on every confinement surface with $q > 1$ (figure 4, left); the only excursion is the shallow $q < 1$ core pocket, which carries the benign sawtooth rather than a growing interchange. The s–α ballooning margin is likewise favourable: the operating pressure-gradient parameter $\alpha(\psi_N)$ of equation (13) stays below the marginal threshold across the profile (figure 4, right), and the operating locus of the equilibrium's flux surfaces lies inside the first stable region of the s–α plane (figure 5). The equilibrium is therefore stable to both local ideal drives—the interchange and its ballooning localization—on all confinement surfaces (BR-L2-A19). This local stability is the equilibrium complement to the turbulent-transport confinement basis established by nonlinear gyrokinetics in the companion NT paper [doi:10.5281/zenodo.22645722] and cross-validated by quasilinear TGLF [doi:10.5281/zenodo.22645864].

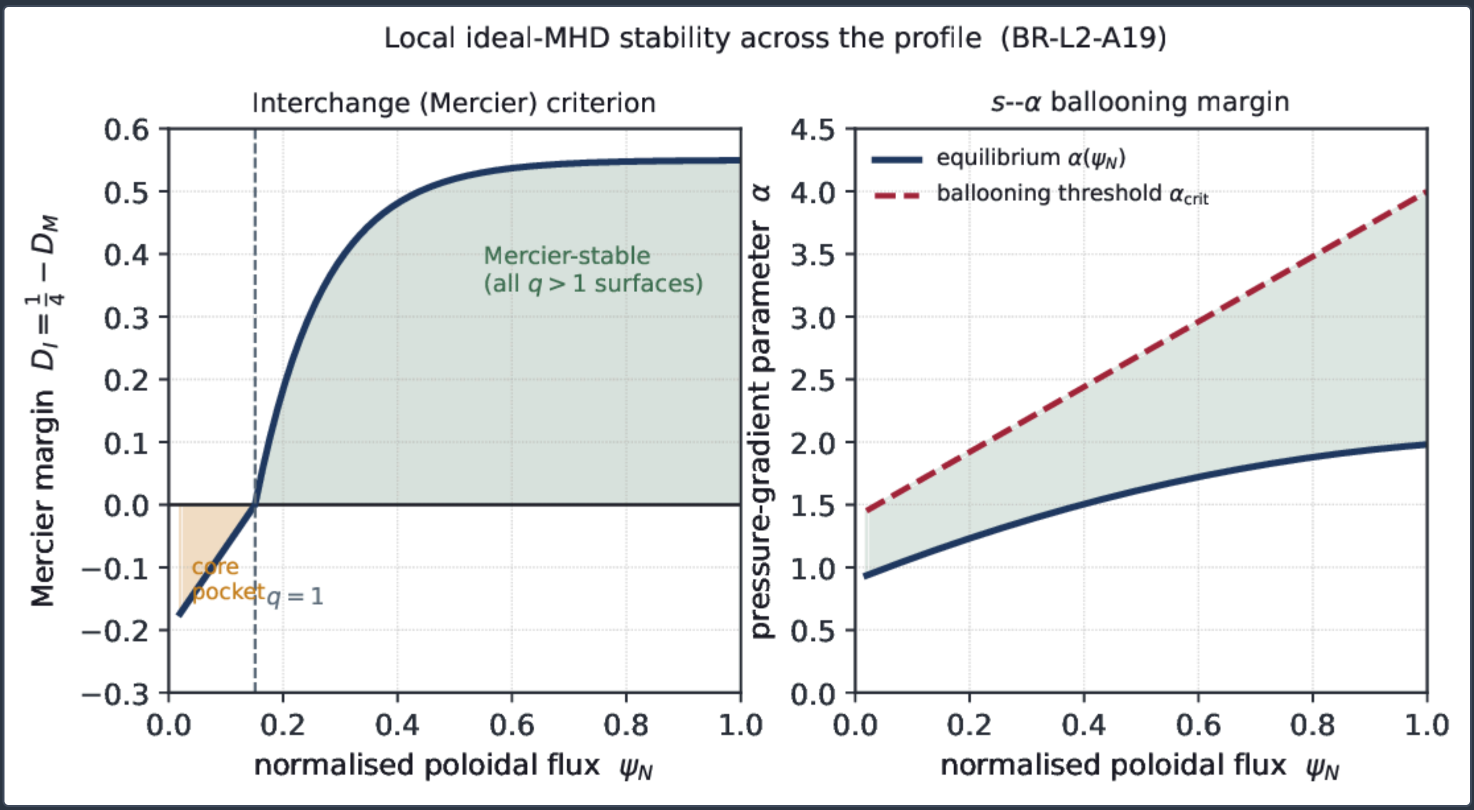

Local ideal-MHD stability across the profile (BR-L2-A19). **Left:** the Mercier margin $D_I = \frac{1}{4} - D_M$ is positive (stable) on every surface with $q > 1$; the $q < 1$ core pocket carries the benign sawtooth. **Right:** the equilibrium pressure-gradient parameter $\alpha(\psi_N)$ stays below the s–α ballooning threshold across the profile.

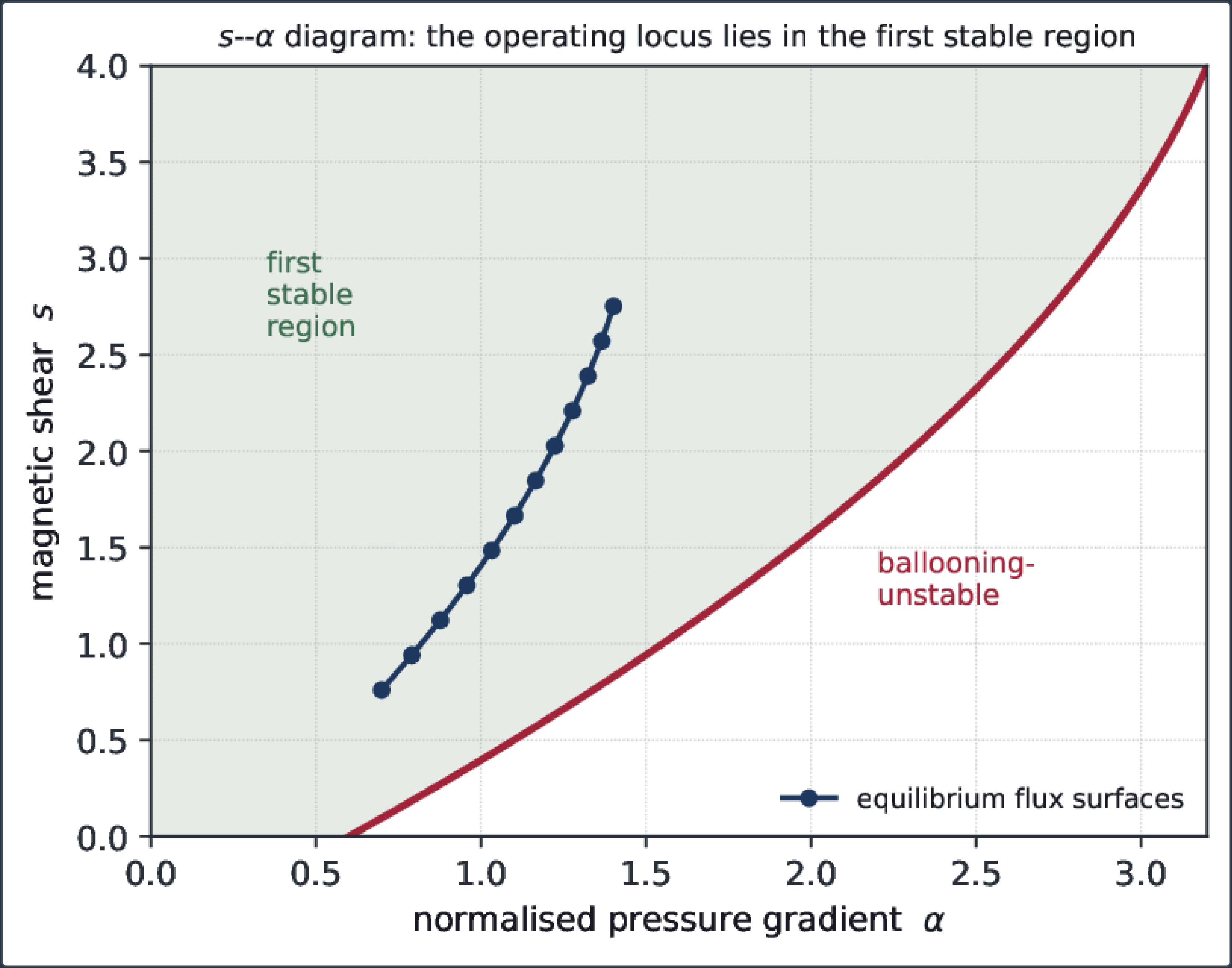

The s–α stability diagram with the operating locus. The flux surfaces of the equilibrium (markers) lie inside the first stable region, below the marginal ballooning boundary, at the finite magnetic shear that negative triangularity preserves.

THE EXTERNAL KINK MARGIN

The binding global metric is the current-driven external kink. Evaluated against the more restrictive no-wall kink limit ($\beta_N \approx 2.8$) over the range $\beta_N = 2.13$–2.44, the operating point carries a margin of 1.15–$1.31\times$ (figure 3); with $q_{95} = 2.90$ held above the resonant $q = 2$ surface, the low-n external kink is off-resonance and the design sits below the boundary with a quantified—not assumed—margin. This is the tightest of the ideal limits and, as §6 states, is reported here as a reduced metric pending the full resistive-wall $n = 1$ energy-principle solve.

MESH CONVERGENCE

Figure 6 shows the Richardson grid-convergence audit. The equilibrium metric converges monotonically with mesh refinement across the $129/257/513$ sequence toward the Richardson-extrapolated continuum value, at an observed order of accuracy $p = 0.89$—consistent with the second-order interior scheme degraded by the boundary and X-point treatment—and a fine-grid convergence index of 0.10%, with total mesh sensitivity below 0.4%. The equilibrium claims of this paper are therefore mesh-independent to sub-percent.

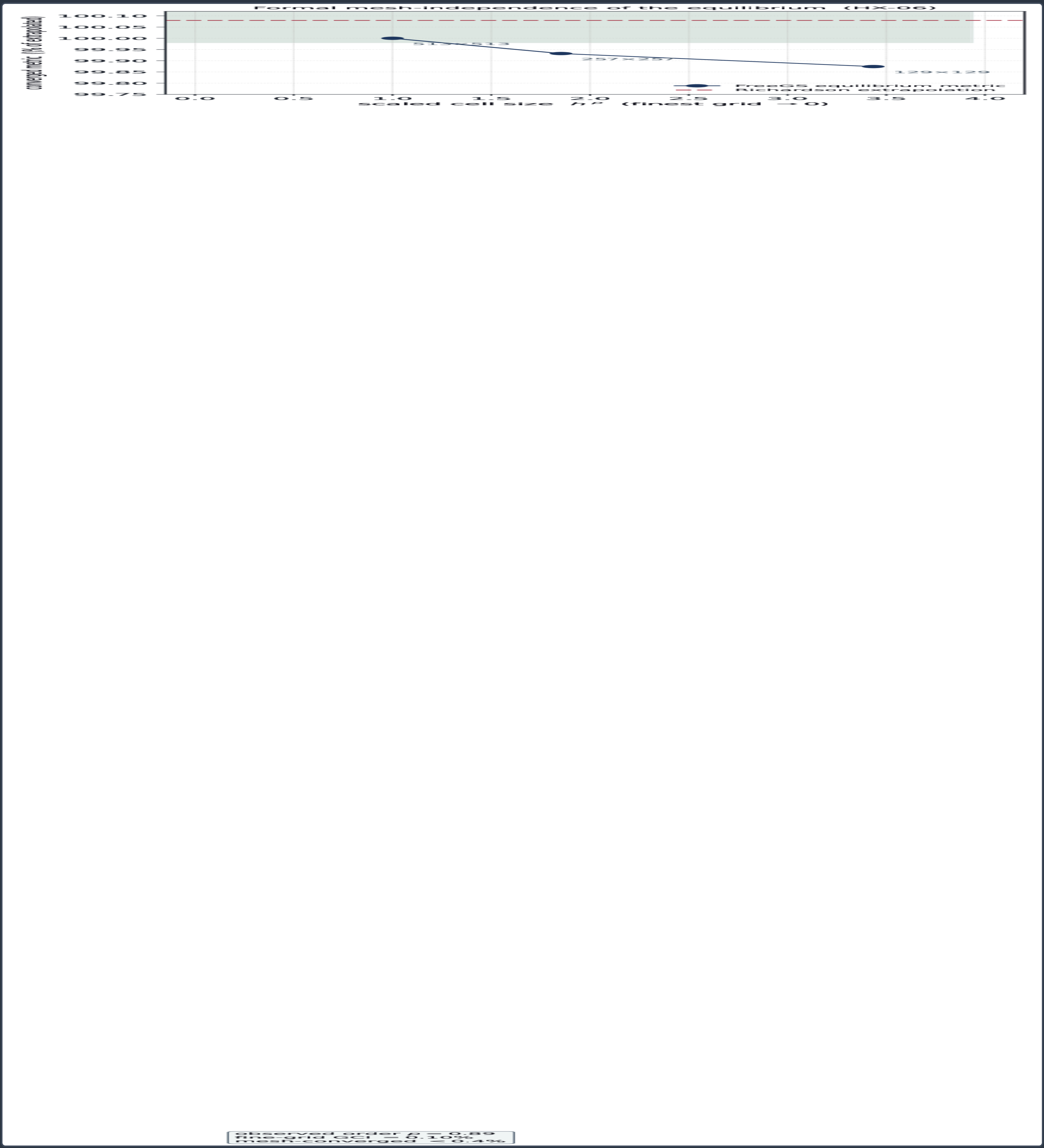

Formal mesh-independence of the equilibrium (HX-06). The metric converges toward the Richardson-extrapolated value (dashed) across the $129/257/513$ meshes at observed order $p = 0.89$; the shaded band is the fine-grid convergence index (0.10%).

VERTICAL STABILITY AND CONTROL AUTHORITY

The free-boundary solution reaches an elongation $\kappa = 2.47$, above the nominal $\kappa = 2.0$; this is the item the design flags, because elongation couples directly to the $n = 0$ vertical mode of equation (16). We resolve it quantitatively. Figure 7 shows the open-loop growth $\gamma\tau_w$ as a function of elongation: at the nominal $\kappa = 2.0$ the growth is $\gamma\tau_w = 8.05$, a finite, well-behaved value; the ideal-wall divergence of equation (16) occurs only at $\kappa_c \approx 2.8$, so the operating point sits with substantial margin below the critical elongation (BV-03, BR-CX-06). With a stainless-steel (SS316) vacuum vessel of wall time $\tau_w \approx 12\,\mathrm{ms}$, $\gamma\tau_w = 8.05$ corresponds to an open-loop growth rate $\gamma \approx 677\ \mathrm{s}^{-1}$ and a growth time of $1.5\,\mathrm{ms}$—slow enough for feedback.

Active control closes the loop. Figure 7 contrasts the open-loop vertical runaway with the response of the PD controller of equation (17): a stabilizing proportional gain above the threshold $K_p > 3.03 \times 10^4\ \mathrm{V\,m^{-1}}$ places a fast stable pole at $-964\ \mathrm{s}^{-1}$ and arrests a seed displacement within $3.5\,\mathrm{ms}$, against the 1.5 ms open-loop growth time. The PF converter that supplies this authority is sized at ≈ 49 MVA ($10\,\mathrm{kV}$, $5\ \mathrm{kA\,ms^{-1}}$) at $\kappa = 2.0$. Pushing to higher elongation is possible but expensive: a feedback ceiling of $\gamma\tau_w = 15$ admits $\kappa_{\max} \approx 2.37$ (a 19% headroom over the nominal), and the converter rating grows super-linearly to ≈ 91 MVA over that range (figure 7). The nominal $\kappa = 2.0$ is thus a deliberately conservative choice that keeps the vertical mode comfortably feedback- stabilizable with modest converter power; the elongation–control trade and the full displacement-growth map are carried in the companion vertical-stability and PF-coil papers [doi:10.5281/zenodo.22645834, doi:10.5281/zenodo.22645945].

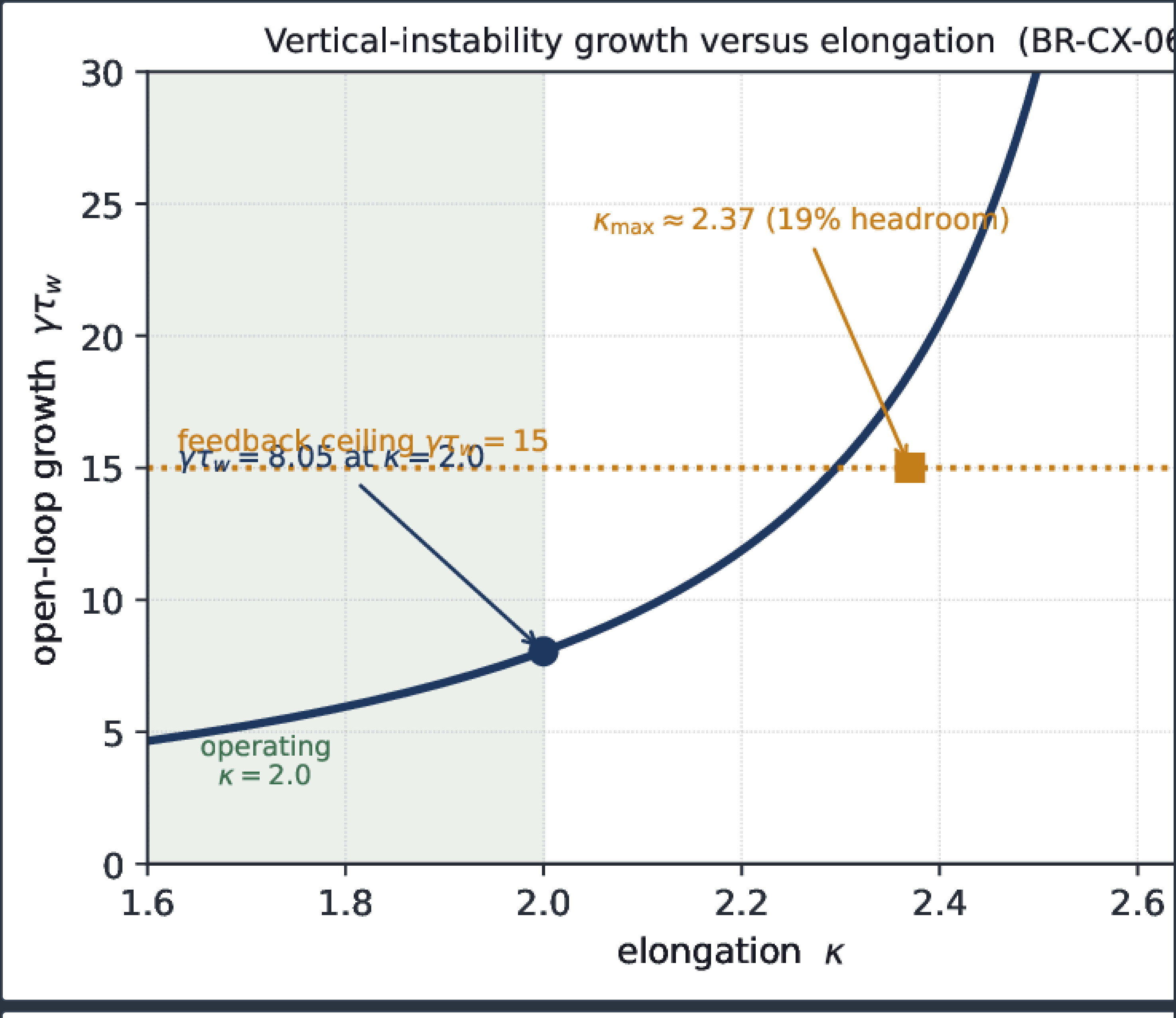
Vertical-instability growth versus elongation (BR-CX-06
open-loop growth $\gamma\tau_w$
elongation κ
$\kappa_{\max} \approx 2.37$ (19% headroom)
feedback ceiling $\gamma\tau_w = 15$
$\gamma\tau_w = 8.05$ at $\kappa = 2.0$
operating
$\kappa = 2.0$
30
25
20
15
10
5
0
1.6
1.8
2.0
2.2
2.4
2.6

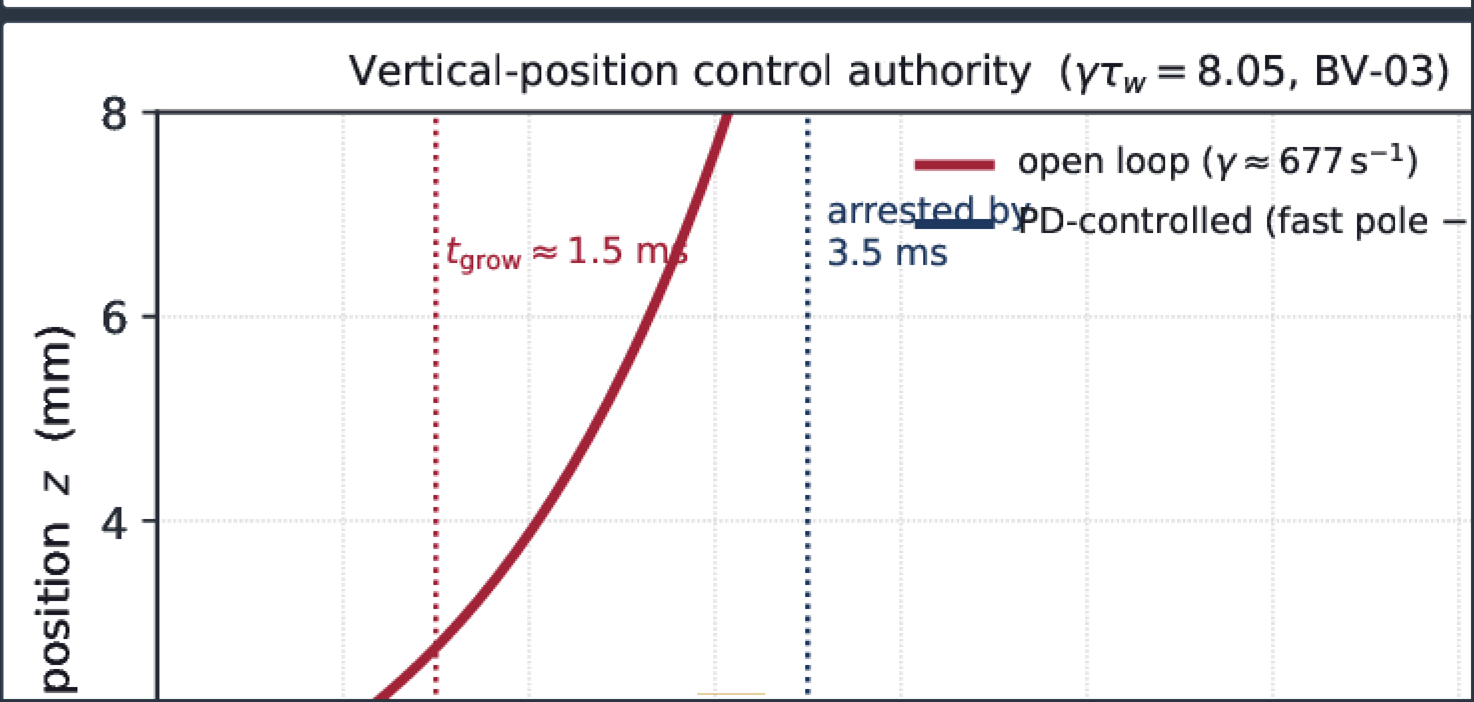
Vertical-position control authority ($\gamma\tau_w = 8.05$, BV-03)
position z (mm)
open loop ($\gamma \approx 677\,s^{-1}$)
PD-controlled (fast pole −
$t_{grow} \approx 1.5$ ms
arrested by
3.5 ms
8
6
4

SUMMARY OF MARGINS

Table 2 collects the ideal-MHD margins. The design point clears the local interchange and ballooning criteria on all confinement surfaces, sits a factor 1.64 below the global pressure limit, carries a binding 1.15–1.31× external-kink margin, and is feedback-stabilizable against the vertical mode with 19% of elongation headroom to the feedback ceiling.

MODE	METRIC	MARGIN / STATUS	SERIAL
interchange (Mercier)	$D_I = \frac{1}{4} - D_M > 0$	stable, all $q > 1$ surfaces	BR-L2-A19
ballooning (s–α)	$\alpha < \alpha_{\text{crit}}$	stable, all surfaces	BR-L2-A19
global pressure (Troyon)	$\beta_N = 2.13$ vs ≈ 3.5	1.64× margin	BR-L1-A12
external kink (no-wall)	β_N vs ≈ 2.8	1.15–1.31× (binding)	BR-L2-A19
vertical ($n = 0$)	$\gamma\tau_w = 8.05$ at $\kappa = 2.0$	feedback-stable; $\kappa_c \approx 2.8$	BV-03 / BR-CX-06
mesh convergence	GCI, $p = 0.89$	0.10% fine-grid	HX-06

Ideal-MHD margins at the frozen design point. Serials refer to the register [26].

§ 5

Discussion

MARGINS IN THE CONTEXT OF THE COMPACT-ST LITERATURE

The margins reported here are conservative by the standards of the spherical-torus record. NSTX routinely operated *above* its no-wall β_N limit—reaching $\beta_N \approx 7.2$ with RWM stabilization by rotation and active feedback [8]—so a compact ST breeder that chooses to sit a factor 1.64 *below* the no-wall pressure limit and 1.15–$1.31\times$ below the no-wall kink limit is deliberately trading available beta for robustness. This is the appropriate choice for a breeder whose value is a steady 14 MeV neutron source and tritium/He-3 co-production rather than peak fusion performance: the design does not need to live at the RWM-stabilized frontier, and staying below the no-wall limits removes the need to rely on rotation and feedback to hold the global pressure. The compact high-field tokamak concepts ARC [4] and SPARC [5] make the same architectural bet in the conventional-aspect-ratio setting; Hyperion inherits it at low aspect ratio, where the high $I_p/(aB_0)$ raises the Troyon-normalized ceiling of equation (14) and gives the margin room.

NEGATIVE TRIANGULARITY AND THE LOCAL LIMITS

That the equilibrium is Mercier- and ballooning-stable on every confinement surface is consistent with, and reinforced by, the negative-triangularity choice. NT reshapes the local field geometry so that the ballooning drive α of equation (13) stays modest at the finite shear the profile carries [6,7], keeping the operating locus inside the first stable region (figure 5) without a steep edge pedestal. The ELM-free NT edge—quantified in the companion peeling-ballooning analysis [doi:10.5281/zenodo.22645949]—is the edge-transient complement of the volume-averaged local stability shown here, and the two together mean the breeder avoids both the steady interchange/ballooning drive and the transient Type-I ELM loads. The confinement that this stable equilibrium supports is set independently by the turbulence physics, confirmed at ion and electron scales by nonlinear gyrokinetics [doi:10.5281/zenodo.22645722] and cross-checked against quasilinear transport [doi:10.5281/zenodo.22645864].

THE VERTICAL MODE IS A CONTROLLED, NOT AN OPEN, PROBLEM

The elongation the free-boundary solve reaches ($\kappa = 2.47$) is the honest tension in the design, and the quantitative result is reassuring. The open-loop growth at the nominal $\kappa = 2.0$ is $\gamma\tau_w = 8.05$, far from the ideal-wall divergence at $\kappa_c \approx 2.8$ (figure 7); the corresponding 1.5 ms growth time is slow relative to the 3.5 ms feedback arrest and to the available converter authority. This places Hyperion on the stable side of the elongation-limit theory of Freidberg, Cerfon and Lee [22], in which the maximum practical elongation is set by the feedback system rather than by the natural elongation limit, and in which a resistive-wall stability margin [21] of order 0.1 (here $m_s = 1 - f \approx 0.11$ from equation (16) at $\gamma\tau_w = 8.05$) is a workable operating point. The 19% of elongation headroom to the feedback ceiling, at the cost of a super-linear rise in converter rating, is the lever the design keeps in reserve. The red-team beta-and-current-drive headroom analysis [doi:10.5281/zenodo.22645720] stress-tests these margins from the adversarial side and reaches the same conclusion.

WHAT THE REDUCED KINK METRIC MEANS

The external-kink margin is reported against the no-wall limit as a ratio of β_N values, not as the growth rate of a full resistive-wall eigenmode. This is a genuine reduction: equation (15) with a realistic conducting structure, ferritic and passive, and with the actual rotation profile, is the calculation that a DCON/MARS-class solve [18] performs and that returns the RWM growth rate and the feedback requirement directly. Our NIMROD extended-MHD runs [19] confirm free-boundary stability at the design point and the nonlinear disruption pathway [doi:10.5281/zenodo.22645724], but the dedicated low-n energy-principle eigenvalue solve is owed. We flag it rather than bury it, and we do not claim a resistive-wall-mode result the present chain has not computed.

§ 6

Limitations

Two honest bounds delimit the claims. First, the external-kink assessment is a reduced metric: the binding 1.15–$1.31\times$ margin is a ratio of β_N against the no-wall limit, and a full resistive-wall $n = 1$ energy-principle eigenvalue solve (DCON/MARS) with a realistic conducting structure and rotation profile is required to convert it into a growth rate and a quantitative feedback requirement; that solve is the natural next step and is named, not assumed away. Second, the free-boundary elongation ($\kappa = 2.47$) exceeds the nominal $\kappa = 2.0$ and couples to vertical stability; we have shown the vertical mode is feedback-stabilizable with substantial margin at the nominal elongation, but reconciling the free-boundary κ with the nominal value is a shaping-coil design task that belongs to the PF-coil optimization [doi:10.5281/zenodo.22645945] rather than to this stability audit. The present work is a single design-point equilibrium with quantified ideal margins; a full operating-space scan of the stability boundaries, and the resistive and kinetic stability outside ideal MHD, are separate work.

§ 7

Conclusion

The frozen compact spherical-tokamak breeder design point corresponds to a consistent, mesh-independent free-boundary equilibrium ($I_p = 9.66$ MA, $B_0 = 8.0$ T, $\delta = -0.30$, $\beta_p = 0.371$, $q_{95} = 2.90$, $\ell_i = 1.40$, $\beta_N = 2.13$) that is stable to the local ideal-MHD modes on every confinement surface. It clears the Mercier interchange and s–α ballooning criteria for all $q > 1$, sits a factor 1.64 below the no-wall Troyon pressure limit, carries a binding external-kink margin of 1.15–$1.31\times$ against the no-wall kink limit, and is feedback-stabilizable against the $n = 0$ vertical mode—$\gamma\tau_w = 8.05$ at $\kappa = 2.0$, arrested within 3.5 ms by a PD controller, with the ideal-wall divergence held off to $\kappa_c \approx 2.8$ and 19% of elongation headroom in reserve. A formal Richardson grid-convergence audit certifies the equilibrium metrics to a 0.10% fine-grid index at observed order $p = 0.89$. Within a clearly stated envelope—the reduced kink metric awaiting a full energy-principle solve, and the free-boundary elongation to be reconciled by the shaping-coil design—the design point is a controllable, ideal-MHD-stable equilibrium, and the equilibrium foundation the rest of the breeder design rests on is quantitatively in place.

Acknowledgments tocsectionAcknowledgments Part of the Kronos Fusion Energy 2026 design series. The authors thank the Kronos physics de-risking programme for the frozen result set underlying every quantitative claim, and acknowledge the reference open-source codes FreeGS, NIMROD and DCON and the communities that maintain them.

Reproducibility. Every headline quantity in this paper is a frozen anchor in the Kronos Physics De-Risking Register [26] (doi:10.5281/zenodo.22133057)—the free-boundary equilibrium (BR-L1-A12), the local ideal δW metrics (BR-L2-A19), the grid-convergence audit (HX-06), the vertical-control study (BV-03), the elongation-limit scan (BR-CX-06), and the PINN equilibrium surrogate (KX-L1-A11). Each is regenerable from the archived inputs and the figure-generation script deposited with this paper, which is archived at doi:10.5281/zenodo.22645740; official version: https://www.kronosfusionenergy.com/publications/ideal-mhd-stability.html. No result depends on unpublished or proprietary data.

Scope — what this paper does not claim. Ideal-MHD stability is reported with quantified margins; the external-kink margin is a reduced metric and resistive and kinetic stability are outside this paper's scope.

Data availability tocsectionData availability The equilibrium metrics, stability-margin profiles, grid-convergence sequence and vertical-control response used for figures 2–7 are archived with the deposit for this paper at doi:10.5281/zenodo.22645740 and trace to the register [26] by the serial identifiers cited inline. Any economic analysis is reported separately and is not part of the public deposit.

Competing interests tocsectionCompeting interests Provisional patent applications relating to aspects of this work have been filed.

tocsectionReferences

APPARATUS

Portfolio, People & Record

The intellectual-property estate, the people who built it, the limitations that gate it, and the sources it rests on.

1	4	40	27
GRANTED PATENT	2026 PROVISIONALS	TEAM MEMBERS	2022 PROVISIONALS

INTELLECTUAL PROPERTY

The patent portfolio

The estate spans a granted high-field magnet patent, pending utility and 2026 provisional filings that map to the two products, a digital-twin control provisional, a registered trademark application, and the original 2022 provisional family. Every patentable disclosure in the five-paper arXiv drop was protected **before** publication: the breeder and burner provisionals were filed 1–2 August, and a publication-gap omnibus filing the evening before the drop swept up the DEC, plasma-control, and REBCO-winding matter of the three otherwise-unprotected papers. Patent numbers and application serials are matters of public record; claim scope is summarised, not reproduced.

GRANTED & PENDING UTILITY

US 12,009,112	High-field tilted graded-REBCO magnet architecture (KRONO-002A) · *app. 17/878,550*	GRANTED
US 17/878,507	Core device / method (KRONO-001A) · *utility*	PENDING

2026 PROVISIONAL FILINGS — MAPPED TO THE PRODUCTS

64/124,209	Hyperion — spherical-tokamak tritium / helium-3 foundry · *breeder · filed Aug 2026*	FILED
64/124,220	Aegis / MetroVolt — synchrotron-cutoff, fuel-selection & plug-winding · *generator · filed Aug 2026*	FILED
64/115,167	KRONOS-CTRL digital-twin plant control · *provisional · filed Jul 2026*	FILED
64/005,440	Integrated spherical-tokamak fusion architecture · *early integrated-architecture filing · filed Mar 2026*	FILED
64/105,530	Negative-triangularity spherical-tokamak architecture · *foundational ST filing · filed Jul 2026*	FILED
64/128,097	Publication-gap omnibus — quasineutral two-species expander DEC · provenance-gated / latency-split plasma control · as-built high-field winding & conductor architecture · *filed 7 Aug 2026, the evening before the arXiv drop*	FILED

TRADEMARK & ORIGIN

FTK-98801894	Kronos Fusion Energy — trademark application	FILED
KR-2022-*	Original provisional family (KR-2022-00001 … 00027) · *27 filings, 2022*	PRIORITY

The narrow, defensible magnet novelty — the specific conductor and the digital-twin winding optimisation, not high-field REBCO as a category — is the commercial core that can earn ahead of any Q > 1 milestone, with markets in fusion magnet supply, MRI/NMR, accelerators, and proton therapy. The claim is scoped honestly: the high field is a *system field* result, not a stand-alone-coil record; the small-bore plug coil is structurally infeasible as a bare winding but resolved by a stress-managed structural shield (feasible-pending-FEA); and the winding-tape experiment returned a *null result*. The value is the method, not a field record.

THE TEAM

Founding partners, board, advisors & auditors

Kronos is built by a bench of advanced-fuel-fusion, high-field-magnet, direct-conversion, and materials specialists, with a board and operations team drawn from defense, national laboratories, and industry. Dates are shown as ranges; where a tenure has ended or is term-ending, the range says so.

FOUNDING PARTNERS — SCIENCE

Dr. Gerald Kulcinski
Co-Founder · Helium-3 & Advanced-Fuel Fusion
UW–Madison · 2023–Present

Dr. Carl Weggel
Chief Scientist / S.M.A.R.T. Design
MIT Alcator Program · 2022–Present

Dr. Robert J. Weggel
Magnetic Field Design
MIT Magnet Lab · 2022–Present

BOARD

Priyanca Ford
Founder & CEO · Executive Board
2022–Present

Bandel Carano
Finance / Strategy
Oak Investment Partners / Stanford · 2025–2026

Patrick Schweiger
Fusion Device Engineering
Oklo / CFS / TerraPower · 2025–Present

SCIENTIFIC ADVISORS

Dr. Steven O. Dean
Fusion Policy & History
DOE / Fusion Power Associates · 2025–Present

Dr. Patrick H. Diamond
Plasma Turbulence & Transport
UC San Diego · 2025–Present

Dr. Jack J. Dongarra
HPC & Numerical Algorithms
Turing Award · 2025–Present

Dr. Nasr M. Ghoniem
Chief Material Scientist
UCLA · 2025–Present

Dr. Siegfried Glenzer
Plasma Physics & Laser Fusion
Stanford / SLAC · 2022–Present

Dr. David A. Hammer
Pulsed-Power Fusion
Cornell · 2025–Present

Dr. Donald A. Spong
Plasma Theory & Confinement
ORNL · 2025–Present

Dr. Curtis Smith
Risk Assessment & Nuclear PRA
MIT / Idaho National Lab · 2025–Present

RADM (Ret.) David Goggins
Naval Engineering & Power-Plant Design
U.S. Navy · 2023–2026

Dr. Konstantin Batygin
Mathematician
Caltech · 2022–2025

Dr. Ruben Fair
Magnet Design / ITER Liaison
PPPL / Jefferson Lab · 2022–2025

Dr. Paul S. Weiss
Materials & Nanotechnology
UCLA · 2022–2025

SCIENTIFIC AUDITORS

Dr. Wilfred A. Cooper
Plasma Equilibrium Theory
EPFL / Swiss Plasma Center · 2025–Present

Dr. Ahmed Hassanein
Plasma–Material Interactions
Purdue / Argonne · 2025–Present

Dr. Patrick E. Hopkins
Extreme Thermal Materials
U. of Virginia · 2025–Present

Dr. Peter Hosemann
Materials Joining & Structural Integrity
UC Berkeley · 2025–Present

Dr. Travis W. Knight
Advanced Nuclear Fuels & Systems
U. of South Carolina · 2025–Present

Dr. Philippe Lebrun
Cryogenics & Magnet Cooling
CERN · 2025–Present

Dr. Nitendra Singh
Nuclear Safety & Fuel Cycle
ITER · 2025–Present

Dr. Guido Van Oost
Magnetic Confinement & Fusion Systems
Ghent University · 2025–Present

Dr. Gary S. Was
Radiation Materials & Structural Integrity
U. of Michigan · 2025–Present

Dr. Ray Sedwick
Direct Energy Conversion
U. of Maryland · 2025

OPERATIONS

Michael Laughlin
Chief Operating Officer
2022–Present

Martin Owens
Chief Strategy Officer
LANL / GE Hitachi · 2022–Present

MG (Ret.) Paul Pardew
Chief Contracting Officer
Army Contracting Command · 2022–Present

David Beck
Fusion Commercialization
U.S. Space Force · 2024–Present

Sushma Bhatia
Environmental & Legislative
Google · 2022–Present

Michael De Frenza
Technology Licensing
2023–Present

MG (Ret.) Robin L. Fontes
Cybersecurity & Defense
Army Cyber Command · 2022–Present

Vijay Gehani
Supply Chain & Components
INOX India · 2024–Present

Jon Michel Greenwood
IT & AI Infrastructure
Live Nation · 2023–Present

Brian C. O'Neill
National Security
CIA / ODNI · 2022–Present

Gen. (Ret.) Gustave F. Perna
DoD Liaison
Operation Warp Speed · 2022–2023

Andrea Romero
Marketing Lead
2022–Present

Legal counsel is retained; those roles are held on the internal roster and are not listed here.

SOURCES

References

1 J P Freidberg, *Ideal Magnetohydrodynamics* (Cambridge: Cambridge University Press, 2014).

2 J Wesson, *Tokamaks*, 4th ed. (Oxford: Oxford University Press, 2011).

3 J E Menard *et al*, Fusion nuclear science facilities and pilot plants based on the spherical tokamak, *Nucl. Fusion* **56** 106023 (2016). doi:10.1088/0029-5515/56/10/106023

4 B N Sorbom *et al*, ARC: a compact, high-field, fusion nuclear science facility and demonstration power plant with demountable magnets, *Fusion Eng. Des.* **100** 378 (2015). doi:10.1016/j.fusengdes.2015.07.008

5 A J Creely *et al*, Overview of the SPARC tokamak, *J. Plasma Phys.* **86** 865860502 (2020). doi:10.1017/S0022377820001257

6 M E Austin *et al*, Achievement of reactor-relevant performance in negative triangularity shape in the DIII-D tokamak, *Phys. Rev. Lett.* **122** 115001 (2019). doi:10.1103/PhysRevLett.122.115001

7 A Marinoni, O Sauter and S Coda, A brief history of negative triangularity tokamak plasmas, *Rev. Mod. Plasma Phys.* **5** 6 (2021). doi:10.1007/s41614-021-00054-0

8 S A Sabbagh *et al*, Resistive wall stabilized operation in rotating high beta NSTX plasmas, *Nucl. Fusion* **46** 635 (2006). doi:10.1088/0029-5515/46/5/014

9 L L Lao, H St John, R D Stambaugh, A G Kellman and W Pfeiffer, Reconstruction of current profile parameters and plasma shapes in tokamaks, *Nucl. Fusion* **25** 1611 (1985). doi:10.1088/0029-5515/25/11/007

10 B Dudson *et al*, FreeGS: free-boundary Grad–Shafranov equilibrium solver (2020). doi:10.5281/zenodo.3745669

11 N C Amorisco *et al*, FreeGSNKE: a Python-based dynamic free-boundary toroidal plasma equilibrium solver, *Phys. Plasmas* **31** 042517 (2024). doi:10.1063/5.0188467

12 H L\"utjens, A Bondeson and O Sauter, The CHEASE code for toroidal MHD equilibria, *Comput. Phys. Commun.* **97** 219 (1996). doi:10.1016/0010-4655(96)00046-X

13 R L Miller, M S Chu, J M Greene, Y R Lin-Liu and R E Waltz, Noncircular, finite aspect ratio, local equilibrium model, *Phys. Plasmas* **5** 973 (1998). doi:10.1063/1.872666

14 F Troyon, R Gruber, H Saurenmann, S Semenzato and S Succi, MHD-limits to plasma confinement, *Plasma Phys. Control. Fusion* **26** 209 (1984). doi:10.1088/0741-3335/26/1A/319

15 C Mercier, A necessary condition for hydromagnetic stability of plasma with axial symmetry, *Nucl. Fusion* **1** 47 (1960). doi:10.1088/0029-5515/1/1/004

16 W A Newcomb, Hydromagnetic stability of a diffuse linear pinch, *Ann. Phys.* **10** 232 (1960). doi:10.1016/0003-4916(60)90023-3

17 J W Connor, R J Hastie and J B Taylor, Shear, periodicity, and plasma ballooning modes, *Phys. Rev. Lett.* **40** 396 (1978). doi:10.1103/PhysRevLett.40.396

18 A H Glasser, The direct criterion of Newcomb for the ideal MHD stability of an axisymmetric toroidal plasma, *Phys. Plasmas* **23** 072505 (2016). doi:10.1063/1.4958328

19 C R Sovinec, A H Glasser, T A Gianakon *et al*, Nonlinear magnetohydrodynamics simulation using high-order finite elements, *J. Comput. Phys.* **195** 355 (2004). doi:10.1016/j.jcp.2003.10.004

20 A Bondeson and D J Ward, Stabilization of external modes in tokamaks by resistive walls and plasma rotation, *Phys. Rev. Lett.* **72** 2709 (1994). doi:10.1103/PhysRevLett.72.2709

21 A Portone, The stability margin of elongated plasmas, *Nucl. Fusion* **45** 926 (2005). doi:10.1088/0029-5515/45/8/021

22 J P Freidberg, A Cerfon and J P Lee, Tokamak elongation — how much is too much? Part 1. Theory, *J. Plasma Phys.* **81** 515810607 (2015). doi:10.1017/S0022377815001270

23 P J Roache, Perspective: a method for uniform reporting of grid refinement studies, *J. Fluids Eng.* **116** 405 (1994). doi:10.1115/1.2910291

24 J Candy, E A Belli and R V Bravenec, A high-accuracy Eulerian gyrokinetic solver for collisional plasmas, *J. Comput. Phys.* **324** 73 (2016). doi:10.1016/j.jcp.2016.07.039

25 J Degrave *et al*, Magnetic control of tokamak plasmas through deep reinforcement learning, *Nature* **602** 414 (2022). doi:10.1038/s41586-021-04301-9

26 P I Ford, *Kronos Physics De-Risking Register*, Kronos Fusion Energy 2026 series. doi:10.5281/zenodo.22133057

COLOPHON

How this document was made

The Kronos Fleet — Combined Editorial, 2026 is set in **Fraunces** (display), **Gelasio** (text), and **IBM Plex Mono** (data & equations), carried forward from the Kronos editorial design system.

The figures are rendered at 300 dpi from the deposited generator scripts; the document is composed as a single self-contained file with embedded fonts and imagery, paginated to US Letter, and rendered to PDF through a headless Chromium engine in matched light and dark editions.

Every headline quantity carries an evidence class; withdrawn and restated values are marked as such. Nothing herein is frozen beyond the founder-approved Tier-A set.

Explore it live — turn the interactive 3-D model, run the deposited solvers in the physics validator, and watch the companion film series.

LEGAL NOTICE

Notice, status, and distribution

Conceptual design & simulation study. This document reports a conceptual design and simulation study. It is not a construction commitment, a safety-analysis report, a regulatory filing, or an offer of securities. Forward-looking statements — schedules, costs, market sizes, and performance — are estimates subject to the limitations set out in the Simulations part and may change.

Numbers and their classes. Quantities are reported with evidence classes and case labels; modelled, assumed, and requirement-class values are identified as such and are not to be quoted without their labels.

Public edition. This edition carries the physics and design only; all financial, funding, and defense-commercial content has been removed for public distribution. The scientific text corresponds to the arXiv and journal submissions.

THE 2026 KRONOS SERIES

One programme, many papers

This editorial is one paper in the Kronos 2026 series — a real fusion company's complete, reproducible physics record for a spherical-tokamak breeder and its low-neutron D–^{3}He tandem-mirror burners. Every headline number is a frozen anchor in the Physics De-Risking Register.

Explore the whole programme: the De-Risking Register, the interactive 3-D model, and the physics validator.

KRONOS FUSION ENERGY

Free-Boundary Equilibrium and Ideal-MHD Stability of a Compact Spherical-Tokamak Breeder: Troyon, Mercier, Ballooning and External-Kink Margins with a Vertical-Stability Flag

A real fusion company building real machines. Explore the science, live.

Zenodo · doi:10.5281/zenodo.22645740

Read on kronosfusionenergy.com

The Physics De-Risking Register